

PAPER • OPEN ACCESS

Coil geometry effects on scanning single-coil magnetic induction tomography

To cite this article: Joe R Feldkamp and Stephen Quirk 2017 *Phys. Med. Biol.* **62** 7097

View the [article online](#) for updates and enhancements.

You may also like

- [Constricted SUSY from No-Scale -SU\(5\): A "blind spot" for LHC top quark reconstruction?](#)
Tianjun Li, James A. Maxin, Dimitri V. Nanopoulos et al.
- [DEFINING THE "BLIND SPOT" OF HINODE EIS AND XRT TEMPERATURE MEASUREMENTS](#)
Amy R. Winebarger, Harry P. Warren, Joan T. Schmelz et al.
- [Wavelet-transform-based time-frequency domain reflectometry for reduction of blind spot](#)
Sin Ho Lee, Jin Bae Park and Yoon Ho Choi



Introducing SunSCAN™ 3D
The Next-Generation Cylindrical Water Scanning System

Learn more: sunnuclear.com

SunSCAN 3D simplifies beam scanning with SRS-class accuracy and user-centered design. It enables faster, easier workflows, and hyper-accurate dosimetry for today's busy clinics.

SUN NUCLEAR corporation

SunSCAN™ 3D is not available for sale in all markets. ©2022 SunNuclear

Coil geometry effects on scanning single-coil magnetic induction tomography

Joe R Feldkamp^{1,3} and Stephen Quirk²

¹ Kimberly-Clark Corp., Neenah, WI, United States of America

² Kimberly-Clark Corp., Roswell, GA, United States of America

E-mail: jrfeld@kcc.com and squirk@kcc.com

Received 3 March 2017, revised 26 June 2017

Accepted for publication 18 July 2017

Published 11 August 2017



CrossMark

Abstract

Alternative coil designs for single coil magnetic induction tomography are considered in this work, with the intention of improving upon the standard design used previously. In particular, we note that the blind spot associated with this coil type, a portion of space along its axis where eddy current generation can be very weak, has an important effect on performance. The seven designs tested here vary considerably in the size of their blind spot. To provide the most discerning test possible, we use laboratory phantoms containing feature dimensions similar to blind spot size. Furthermore, conductivity contrasts are set higher than what would occur naturally in biological systems, which has the effect of weakening eddy current generation at coil locations that straddle the border between high and low conductivity features. Image reconstruction results for the various coils show that coils with smaller blind spots give markedly better performance, though improvements in signal-to-noise ratio could alter that conclusion.

Keywords: convolution integral, electrical conductivity imaging, multi-layer coil

(Some figures may appear in colour only in the online journal)

1. Introduction

A distinguishing characteristic of the human body is its ability to conduct electricity. Electrical conductivity varies naturally between tissue types, with lowest values in bone, cartilage and fat, and highest values observed in muscle and kidney (Gabriel *et al* 1996). In addition,

³ Author to whom any correspondence should be addressed.



Original content from this work may be used under the terms of the [Creative Commons Attribution 3.0 licence](https://creativecommons.org/licenses/by/3.0/). Any further distribution of this work must maintain attribution to the author(s) and the title of the work, journal citation and DOI.

measurable conductivity differences exist between malignant and normal tissues (Joines *et al* 1994) as well as between normal tissue and benign tumors (Delonzor *et al* 2011, Wang *et al* 2014). The natural variation in normal and diseased human tissue suggests that an imaging technique able to accurately capture these intrinsic conductivity differences would provide a medically important diagnostic tool.

Of all the imaging modalities, magnetic induction tomography (MIT) is ideally suited for conductivity imaging since there is no use of ionizing radiation or contrast agents, the method is noninvasive as well as non-contact, and the instrumentation can be configured sufficiently compact to allow portable or remote use (Al-Zeibak and Saunders 1993, Peyton *et al* 1996, Griffiths *et al* 1999, Korjnevsky *et al* 2000). A potential first application for MIT imaging is in the overall management of breast cancer. At room temperature, normal breast tissue has a conductivity of $\sim 0.1 \text{ S m}^{-1}$ compared to a value of $\sim 0.8 \text{ S m}^{-1}$ in a malignant breast tumor (Joines *et al* 1994). MIT can serve as a complimentary technique to current screening techniques for improved initial diagnosis (Health Quality Ontario 2016) (e.g.- adjunct to MRI, mammography, or digital breast tomosynthesis), used for improved imaging of dense breasts (Hruska 2017), as an imaging guide for needle biopsies (Rhee *et al* 2017), or as a primary post-treatment imaging surveillance tool (Lam *et al* 2017). Finally, due to the nature of MIT hardware and its clinical use, MIT may provide a breast imaging modality for populations in developing and emerging countries or women in remote areas. As promising as this seems, current multi-coil MIT has proven problematic. Successful implementation in the breast cancer management process will require MIT refinements that reduce imager size and coil geometry complexity, as well as increased sensitivity and ease of use.

A recent MIT advance (Feldkamp 2015) uses a single coil consisting of concentric circular loops lying in a common plane, or a very closely spaced set of planes, rather than the more common multi-coil array (Scharfetter *et al* 2006a, 2006b, Wei and Soleimani 2012, 2013, Dekdouk *et al* 2016, Stawicki and Gratkowski 2010). The single-coil approach relies upon a closed-form analytical formula that relates coil inductive loss, due to eddy current formation, to a target's full 3D variation in electrical conductivity. A solution was developed from a perturbative expansion of the electric field in Fourier space, which led to a first-order accurate formula that fully captures 'skin-effects', provided that conductivity is much smaller than $\sim \sqrt{2\pi}/(\mu\nu a^2)$ (μ is magnetic permeability, ν is frequency and a is coil radius). For a coil of radius $\sim 2 \text{ cm}$ receiving 12.5 MHz excitation, conductivity must then be small compared to $\sim 400 \text{ S m}^{-1}$, which limits the analytical solution to media having biologically relevant conductivity. Otherwise, the classical skin-effect behavior would not be properly accounted for, and inversion would not lead to correct conductivity values beneath the usual skin-depth.

With suitable RF excitation, a single coil placed near a target induces eddy currents, which in turn create a secondary field that alters coil impedance (Hoult and Lauterbur 1979, Zaman 1980, Harpen 1988a, 1988b). The real part of coil impedance change appears as a dissipative inductive loss in series with the coil. This inductive loss, which can be measured, is related to the full 3D conductivity distribution of the target via a convolution integral that becomes quantitative in the limit of uniform relative permittivity. Inversion of the convolution integral for a set of inductive loss measurements, as described by Feldkamp (2017), allows reconstruction of the conductivity distribution. Even when relative permittivity is severely non-uniform, inductive loss still varies linearly with conductivity (Feldkamp and Quirk 2017a), permitting image reconstruction to proceed. Nevertheless, contrast can be either enhanced or reduced when permittivity variation significantly exceeds that arising naturally in the body (Feldkamp and Quirk 2016), an issue that is reexamined here.

Early versions of multi-coil MIT consisted of an array of coils that generally remain fixed around a target while transfer impedances between all possible coil pairs are probed. In our

single coil case, the coil must be repeatedly relocated to multiple positions, measuring inductive loss and coil orientation-position along the way—which we refer to here as a scan. In more recent multi-coil implementations of MIT (Dekdouk *et al* 2016), the entire coil array is repositioned to permit a new set of unique measurements—accomplished only in a virtual sense for simulation purposes that allowed assessment of data set size. Because a single coil is much easier to manage while scanning, we envision the single-coil MIT scanning approach to be very useful in remote locations where portability is essential.

All of our previous work has relied upon a single coil design—two layers of concentric circular loops spaced 0.05 cm apart, with each layer consisting of five circular loops. Loops are connected in series and have radii set at 0.4, 0.8, 1.2, 1.6 and 2.0 cm. That design was based upon the desire to create eddy currents over a wide range of length scales, so as to promote the best opportunity to resolve a wider range of features in the midst of noise. Encouraging results obtained while using this ‘reference’ coil have motivated us to return to the task of coil design, with the intent of improving performance—e.g. artifact reduction, improved localization and resolution.

A particular artifact that has appeared in either lab phantoms or virtual phantoms contaminated by noise consists of low conductivity ‘holes’ centrally located within higher conductivity inclusions. Given that our circular coils naturally generate a much weaker field along their axis, we postulate the existence of a coil-axis ‘blind spot’ that leads to ‘hole’ artifacts which are not alleviated even though the coil is repositioned over a target. In the next section, a working hypothesis for circular coil behavior is presented that is meant to uncover the relationship between coil design and the appearance of hole artifacts. Using the convolution kernel as a guide, a suite of seven coils is designed that is meant to deliberately vary the breadth of the blind spot. These seven coils are built and then tested against laboratory phantoms containing features comparable to blind spot size, a strategy meant to more effectively expose blind spot behavior. While reduction of ‘hole’ artifacts is important to our rationale for coil geometry choices, we remain cognizant of the impact that design changes can have on other performance metrics, such as feature depth-resolution.

2. Working hypothesis for coil design

As noted, a single coil consisting of concentric circular wires in a common plane is used as both source and detector, though multiple parallel planes of loops are acceptable if planar spacing is much less than loop radii. RF excitation generates a primary field causing eddy currents in a conductive target, together with an associated, phase-shifted secondary field. The secondary field leads to a change in the real component of coil impedance, which shows up as an additional dissipative resistance in series with the coil—referred to here as an inductive loss. As shown previously (Feldkamp 2015, 2017), the real component of impedance change for a coil located at \vec{c} in the fixed lab frame is conveniently written as a three-dimensional convolution integral over all space:

$$\delta Z(\vec{c}) = \int \sigma(\vec{r}) G(\tilde{\mathbf{R}}^T(\vec{r} - \vec{c})) \, dx dy dz \quad (1)$$

The integrand consists of the full 3D electrical conductivity distribution, $\sigma(\vec{r})$, multiplied by the kernel $G(\vec{r}_c)$, where \vec{r}_c locates the field position relative to the coil center and $\tilde{\mathbf{R}}$ is a rotation matrix that maps a coil frame vector to the lab frame:

$$G(\vec{r}_c) = \frac{\mu^2 \omega^2}{4\rho\pi^2} \sum_{j,k} \sqrt{\rho_j \rho_k} Q_{1/2}(\eta_j) Q_{1/2}(\eta_k) \quad (2)$$

Both \tilde{R} and \tilde{c} are measured during the course of a scan using IR optical tracking technology (Feldkamp and Quirk 2017b, 2017c). The kernel determines the point-wise extent to which conductivity will contribute to the inductive loss integral, and depends on coil geometrical features such as loop radii as well as spatial position and orientation. Arguments for the circularly symmetric toroid (or ring) function $Q_{1/2}$ lie in the interval $1 < \eta < \infty$ and are related to field position by:

$$\eta_j = \frac{\rho^2 + \rho_j^2 + z_c^2}{2\rho\rho_j}; \quad \eta_k = \frac{\rho^2 + \rho_k^2 + z_c^2}{2\rho\rho_k} \quad (3)$$

Using any suitable fixed laboratory coordinate system, other symbols are defined by:

$\sigma(\vec{r})$: Electrical conductivity (real part) at field position: $\vec{r} = (x, y, z)$

ρ_k : Cylindrical radial distance from coil axis to wire loop 'k'

ρ : Cylindrical radial distance from coil axis to field point

z_c : Perpendicular distance from coil plane to field point

μ : Magnetic permeability—considered uniform

ω : Angular frequency

The function $G(\vec{r}_c)$ is rapidly evaluated through use of a hypergeometric series for the toroidal functions (Gradshteyn and Ryzhik 1980). If the coil is not rotated relative to the lab frame, then the rotation matrix is just the identity matrix. As is clear from equation (2), sensitivity increases with the square of excitation frequency, which is set at 12.5 MHz in current instrumentation. Though a higher working frequency may appear preferable, operation above 60 MHz already leads to higher order 'skin-effects' not fully captured by the convolution integral (Harpen 1988a). Coil response varies considerably, though does not typically exceed $\sim 1\Omega$ at 12.5 MHz. Measurement precision is currently no worse than $\sim \pm 0.01\Omega$, as determined by a 'blank' scan over a perfectly insulating target.

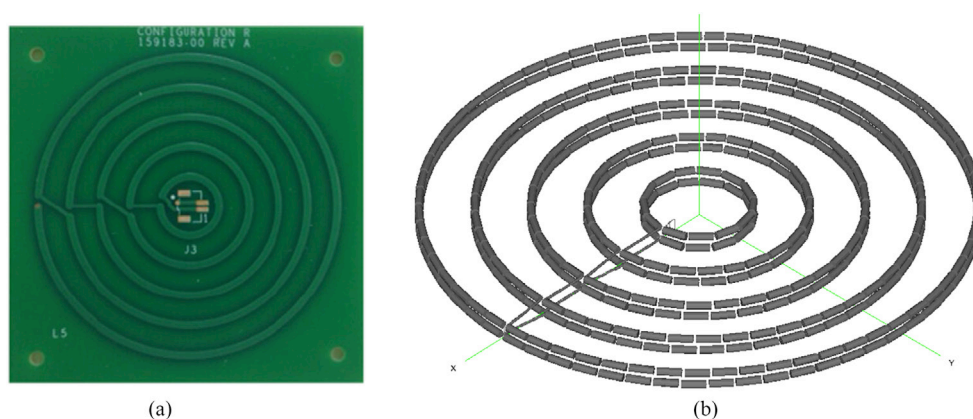
Because of the spatially variant nature of the convolution kernel, not all regions of a specimen contribute equally to a measurement made at a particular coil location and orientation. In fact, while some regions are well sampled, other locations may not be sampled at all. Inadequate sampling during a scan may lead to an increased vulnerability to noise that impairs image reconstruction in poorly sampled regions. This effect can be compared among coil designs that, upon closer examination of the kernel, deliberately vary the size of the 'blind spot'—table 1 provides a listing of seven selected coil designs, while figure 1 illustrates typical coil construction for coil '1', our 'reference' coil from previous work.

For each of the coil designs, the convolution kernel is plotted in figure 2 as a function of the radial distance from the coil axis, on a plane located 0.5 cm from the coil plane—i.e. in the steep portion of the 'decay zone' just above a target ((Feldkamp and Quirk 2017c), figure 11). For each coil, the plot is normalized against the largest kernel value to facilitate easier comparison. Clearly, the coils behave quite differently with regard to their ability to 'sample' space. In all cases, there is a circularly symmetric 'blind spot' centered on the coil's axis, where sampling falls to zero on the axis. Physically, a blind spot is a region where the induction of eddy currents is weak, or even nonexistent when exactly on the coil axis—due to poor sampling. The spatial extent of the blind spot varies from one coil to the next, being least for code '2' and largest for code '7'.

While directly over a highly conductive feature whose dimensions are smaller than the blind spot dimension, very little sampling of the feature is expected. To remedy the situation, sampling could be improved by simply repositioning the coil so that the feature is positioned where the kernel is large. However, in the physically relevant situation that the small feature is completely surrounded by very low conductivity material, inductive loss remains small since

Table 1. List of coils tested against phantoms.

Coil-code	Layers	Loops	Radii (cm)	L(μ H)
#1-reference	2	5	0.4, 0.8, 1.2, 1.6, 2.0	2.16
#2	4	2	0.8, 1.2	1.94
#3	4	2	0.8, 1.4	2.06
#4	4	2	0.6, 1.6	1.91
#5	4	2	0.6, 1.8	2.10
#6	4	1	2.2	2.02
#7	4	1	2.5	2.35

**Figure 1.** Two views of coil #1; (a) PCB—inner side of coil; (b) model—showing radial connectors.

convolution will naturally include contributions that multiply even large kernel values by very small conductivity values just outside of the feature. So in spite of efforts to improve sampling, sufficiently strong eddy currents are not induced in the surrounding low conductivity matrix that would have permitted the high conductivity feature of interest to participate. Thus, noise could frustrate our ability to ‘probe’ the highly conductive feature even when scanning includes coil positions not centered over the feature. Due to convolution then, (both) kernel structure and conductivity distribution are equally important, so that a substantial inductive loss signal requires modest-to-large values for both kernel and conductivity at a ‘sufficient number’ of points within the coil’s field of view.

In addition to blind-spot behavior, figure 3 shows how the kernel function varies with distance from the coil plane at two radial locations—chosen to fall within the span of the square features built into our phantoms described in the next section when the coil is centered over the square. Figure 3 specifically compares the two coils that show the greatest and least blind spot deficiency, as suggested by figure 2. Of interest is the reach or range of interaction for each of these two coils. While the kernel plotted for coil ‘7’ exhibits a relatively slow decay at either radial position, which is desirable, sampling at the innermost radial location may be too weak to be useful at current signal-to-noise ratios. On the other hand, coil ‘2’ appears to offer a compromise, with modest sampling available at either radial location. Even the differences in kernel decay behavior at the two radial locations for coil ‘2’ may offer some advantage for improved depth discrimination. However, its special advantage at depth discrimination may vanish quickly with depth, given that sampling at the inner radial location falls rather

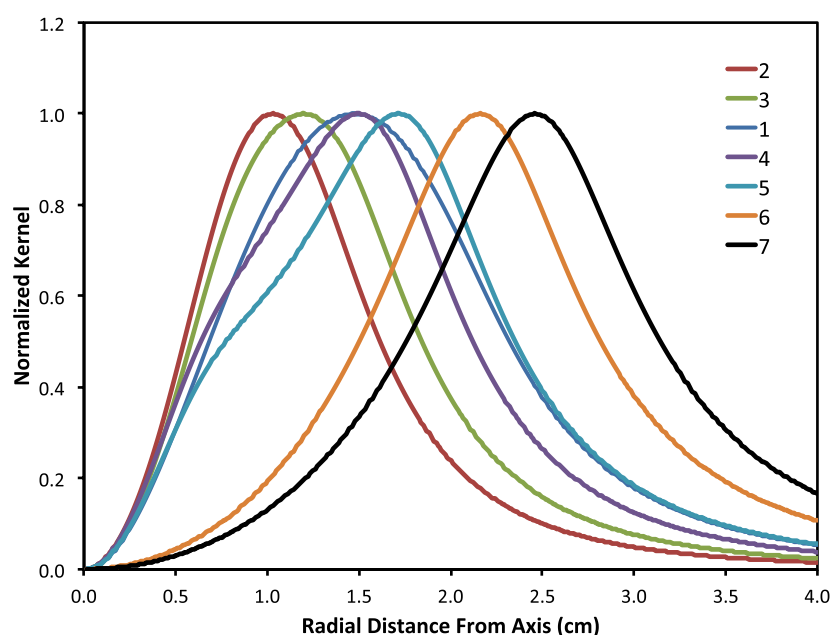


Figure 2. Kernel plotted radially on plane located at $z = 0.5$ cm for all seven coil designs.

quickly below that obtained with coil ‘7’. Thus, any practical rationale for coil selection needs to consider not only blind spot issues, but also how coil design impacts its ability to depth discriminate within some meaningful portion of a target. Here, coil ‘2’ appears to offer better depth discrimination as well as improved blind spot alleviation, attributes that we investigate with lab phantoms.

3. Phantoms used for coil evaluation

To test our hypothesis about the role of ‘blind spot size’ during image reconstruction, we prepared a phantom consisting of a single conductive square plug ($\sim 4.3 \text{ S m}^{-1}$; Play-Doh™ (Jones 1993)) immersed in a medium of low conductivity ($\sim 0.1 \text{ S m}^{-1}$; Agarose (Kandakai *et al* 2012)), all placed in a 14 cm diameter petri dish of 2.4 cm depth. An appendix gives details on independent electrical property measurements made by us at 10 kHz and at frequencies exceeding ~ 60 MHz which indicate that conductivity is essentially flat from DC well into the VHF region of the EM spectrum (appendix, figure A1). The plug has dimensions $4 \text{ cm} \times 4 \text{ cm} \times 2.4 \text{ cm}$ thick, comparable to loop dimensions for our coils. Play-Doh™ was used rather than doped agarose due to its much greater ability to inhibit salt diffusion across the plug boundary—causes boundary smearing. Our intention is to explore how image reconstruction is influenced by coil geometry over a target containing features that fall within the blind spot. Each of the seven coils is alternately attached to our hand-scanning unit and used to acquire data in a free-style scan over the phantom.

Image reconstruction is applied to each of the data sets using a NNLS, SVD-based optimization scheme that uses a weighted, shifted penalty (Feldkamp 2017)—reviewed in later section. The best coil identified from our list of codes is then subjected to a more complex imaging task that involves imaging a phantom comprised of two $4 \times 4 \times 2.4 \text{ cm}$ conductive squares,

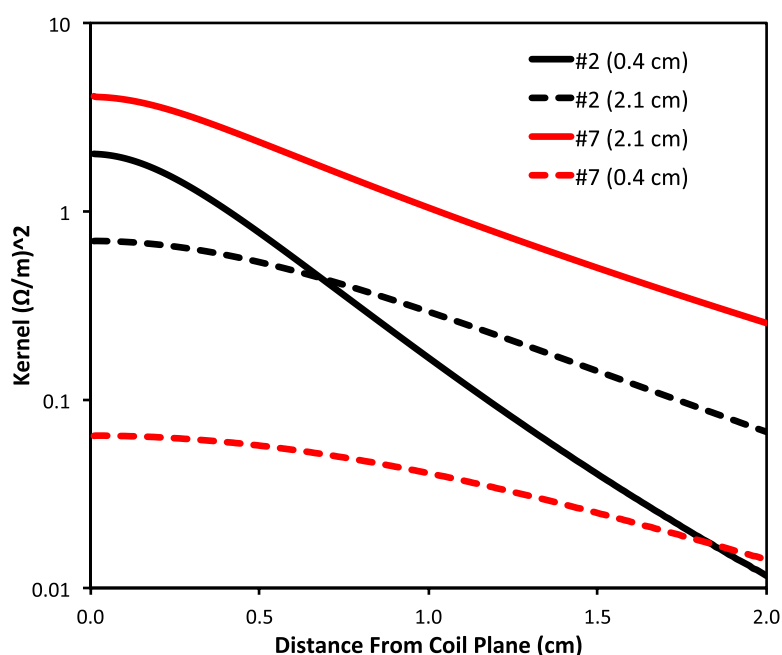


Figure 3. Kernel plotted with distance from coil plane at the radial locations indicated in the plot—the 0.4 cm location falls well inside the feature for a centered coil, while the 2.1 cm location lands at the periphery of the feature for a centered coil.

spaced ~ 2 cm apart. Each square consists of agarose doped with sufficient sodium chloride to give a conductivity of $\sim 1.0 \text{ S m}^{-1}$ (Kandadai *et al* 2012). The squares are immersed in a matrix of rendered animal lard—conductivity $\sim 0.01 \text{ S m}^{-1}$ and relative permittivity⁴ ~ 3.2 . Both phantoms are shown in figure 4. In either case, these two phantoms provide an ample challenge to instrumentation and image reconstruction because of the very low conductivity matrix which inhibits eddy current formation and sampling of the embedded higher conductivity plugs. With reduced eddy currents, signal-to-noise performance is reduced, so that a degree of image degradation is expected. Further improvements in noise reduction and drift suppression are expected to alter the results we find here, as that would enable weaker signals to participate in image reconstruction.

4. Inductive loss measurement

Coil geometry and construction follows that described previously (Feldkamp 2015)—multiple planes of concentric circular loops, spaced either 0.05 cm (2 planes) or 0.03 cm (4 planes), prepared on a multi-layer printed circuit board (PCB). Loop traces are 0.05 cm wide, built from 2 oz. copper, having radii as shown in table 1 and wired in series, giving $N_{\text{layers}} \times N_{\text{loops}}$ total loops. There is a 0.1 cm buildup of PCB material on the side of the coil facing outward, so that there is at least a 0.1 cm separation between coil and target. Coil inductance, L , is calculated from equations (5) and (6) of earlier work (Feldkamp 2015)—the latter repeated here in more general form in terms of loop self-inductance, L_{sj} , and mutual inductances between loops, M_{jk} :

⁴Measured with Agilent, model 16451B test fixture.

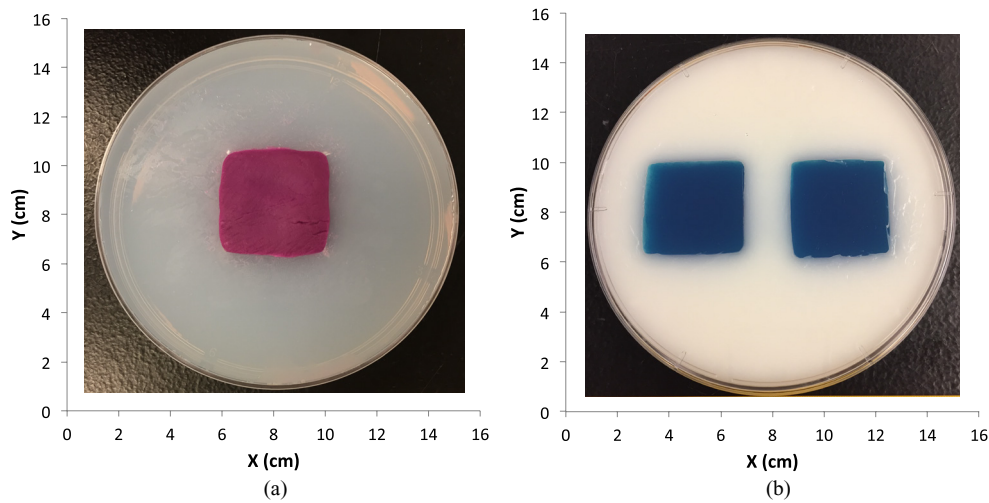


Figure 4. (a) Phantom consisting of conductive square feature ($\sim 4.3 \text{ S m}^{-1}$; $\epsilon_{\text{rel}} \sim 35$), immersed in agarose gel ($\sim 0.1 \text{ S m}^{-1}$; $\epsilon_{\text{rel}} \sim 75$); (b) phantom consisting of two conductive agarose squares ($\sim 1.0 \text{ S m}^{-1}$; $\epsilon_{\text{rel}} \sim 75$) immersed in rendered animal lard ($\sim 0.01 \text{ S m}^{-1}$; $\epsilon_{\text{rel}} \sim 3.2$). For either phantom, the Z axis increases out of the page, starting with $Z = 0$ at the bottom of the petri dish.

$$L = N_{\text{layers}}^2 \left(\sum_{j=1}^{N_{\text{loops}}} L_{sj} + \sum_{j,k=1}^{N_{\text{loops}}} M_{jk} \right) ; j \neq k \quad (4)$$

In this work, there are two or four layers, so that a factor of 4 or 16, respectively, multiplies each sum. Equation (4) is a reasonable approximation for our coil's inductance provided that the distance between layers is very small compared with loop radii. Inductance for coil '1' was calculated to be $2.155 \mu\text{H}$, which agrees with measurement to within 1% (Feldkamp 2015). Thus, the calculated inductance values shown in table 1 are used here.

Coil loss is computed from a change in the real part of admittance, δY_{re} , relative to the free space value, which subtracts the effect of any loss intrinsic to the coil. Given inductance L and frequency ω , coil loss is computed from the formula ((Feldkamp 2015), equation (4)):

$$\delta Z = \omega^2 L^2 \delta Y_{\text{re}} \quad (5)$$

Thus, two admittance measurements are needed—one in free space that avoids interaction with nearby conductive objects, and then subsequent measurements in the immediate vicinity of a conductive specimen. When making 20 to 30 free space measurements at 12.5 MHz, admittance standard deviation is typically $\sim 0.11 \mu\text{S}$ —this leads to a loss precision of $\pm 0.003 \Omega$. However, other issues, most importantly drift, conspire to limit precision to $\pm 0.01 \Omega$. Additional details are found in Feldkamp (2015)—in particular, the approach for measuring phase angle difference between voltage and current in the induction coil.

5. Single-coil scanning methods

Our previous enclosure used to house coil-sensing electronics was modified to permit attachment of a small mast that supports an optical body from NDI (Northern Digital, Inc.) (Wiles

et al 2004). The optical body consists of IR reflective spheres residing in a common plane that are tracked by a remote sensor which reports position of each sphere as well as body orientation—via quaternions. The plane of the optical body is perpendicular to the coil plane so that knowing the orientation of the optical body immediately allows us to know coil orientation. After performing the pivot procedure described in Feldkamp and Quirk (2017b), the position and orientation data acquired during a scan allow us to track the position of the coil center to within ± 0.03 cm (Feldkamp and Quirk 2017c), and orientation to within $\pm 0.5^\circ$, which agrees with the specifications supplied by NDI.

Hand-held scanning can be accomplished in either of two ways. One uses a start-stop movement of the coil while acquiring inductive loss and position data at some predetermined number of random locations (e.g. ~ 135 positions). A more efficient ‘nonstop’ approach moves the coil continuously while acquiring ~ 500 samples ‘on the fly’ along a quasi-random path, as shown in figure 5. Since image reconstruction yielded a very similar coil ranking in either case, only results using the automatic type scan are shown here. After practice, and with the aid of ‘petri markers’, the scan path shown in figure 5 was found to be repeatable, and therefore used for all scans in this work. We are still investigating the role of sampling methodology on image quality, which is planned for a later publication. Optical tracking also allowed us to locate the upper boundary of the target, which is used during meshing.

The scan points illustrated in figure 5 are collected from a common plane, just above the petri dish. For the case shown, involving coil ‘2’, the coil center is located on average at $Z = 2.69$ cm ± 0.075 cm—note that the upper boundary of the petri is located at ~ 2.5 cm. Though moving the coil to locations more distant from the target is usually encouraged, sampling along a nearly common plane without rotation provides the best opportunity for distinguishing ‘blind spot’ misbehavior among codes tested here. Thus, sampling is nearly planar, even though others have shown the importance of coil positioning to improved MIT image reconstruction (Gürsoy and Scharfetter 2009).

6. Image reconstruction algorithm

Discretizing the convolution integral of equation (1) on a finite element mesh leads to a prediction of coil loss, $\tilde{A}\vec{\sigma}$, that approximates the measured loss, \vec{b} . The mesh consists of 15 060 deformed prismatic elements over six layers, spanning a region $16.5 \times 16.5 \times 2.5$ cm, while elemental integrals were computed using a 9-point quadrature rule (Lapidus and Pinder 1982). The number of unknown nodal conductivities on the mesh will greatly exceed the number of inductive loss measurements, so that solution requires the use of penalized non-negative least squares:

$$\min \frac{1}{2} \left\| \tilde{A}\vec{\sigma} - \vec{b} \right\|_2^2 + \frac{1}{2} \tau^2 \left\| \tilde{D} \left(\vec{\sigma} - \vec{\beta} \right) \right\|_2^2 \quad s.t. \quad \vec{\sigma} \geq 0 \quad (6)$$

Diagonal regularization matrix \tilde{D} , with elements $d_j > 0$, allows a depth-dependent penalization of specific nodal conductivity values, computed in our application as:

$$d_j = \exp(-\eta z_j / z_{\max}) \quad (7)$$

Finite element mesh thickness is given as z_{\max} , while z_j is node depth beneath the target boundary. Decay parameter η is set to match the rolloff characteristic of the kernel function, as illustrated in figure 3 for coil ‘2’ and ‘7’.

Vector $\vec{\beta}$ is chosen as the single, uniform conductivity value that best predicts inductive loss. Setting a higher penalty for a particular solution component forces the conductivity to remain closer to the corresponding component in $\vec{\beta}$. Solution to minimization problem (6) is

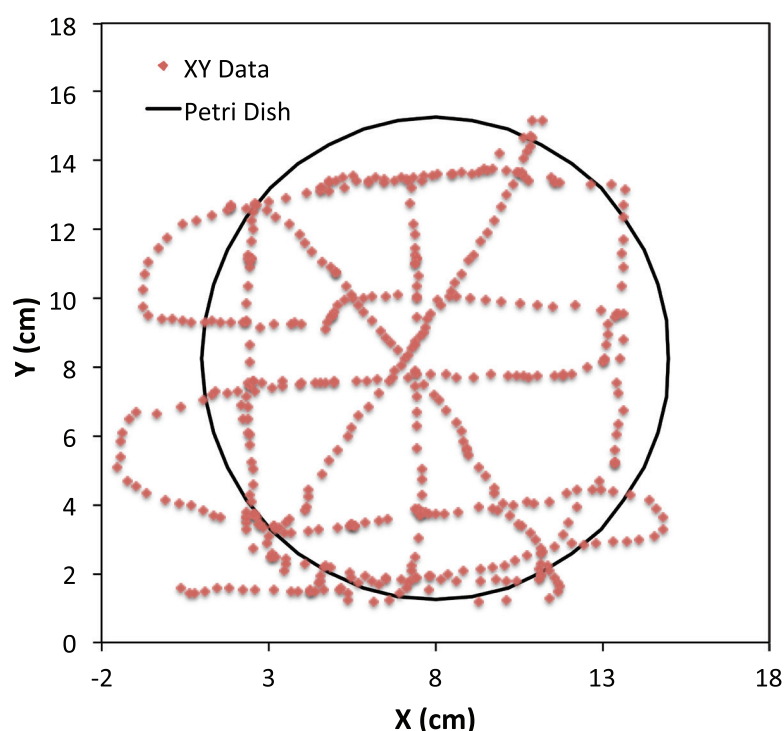


Figure 5. Illustrative sampling pattern for a scan completed in automatic mode, with 497 points collected ‘nonstop’ while scanning with coil ‘2’. As this pattern was found to be repeatable, each scan was obtained similarly.

pursued by a direct method involving active sets (Feldkamp 2017). The global regularization parameter τ is chosen as the singular value obtained from the singular value decomposition of $\tilde{A}\tilde{D}^{-1}$ that yields a prediction error norm \approx measurement error norm associated with the inductive loss measurement vector (discrepancy principle, Donatelli *et al* (2012)). Stepping through the singular values from largest to smallest, perhaps jumping over several at a time, leads to a progressively smaller prediction error. However, this process must be stopped when prediction error approaches the known root mean square error associated with the inductive loss vector. For each singular value tested, the active set method requires five iterations or less to satisfy the KKT (Karush–Kuhn–Tucker) conditions (Kuhn and Tucker 1951, Feldkamp 2017).

7. Results for single-feature phantom

Figure 6 shows a set of X-normal slices passing through the center of the first phantom, for all coils except ‘7’, which is very similar to that obtained for ‘6’. Ideally, the slices should show the presence of the central, highly conductive square feature from top to bottom. Only coil design ‘2’ succeeds completely in that regard, though coil ‘3’ manages to outperform the remaining designs. The trend seen here supports the notion that a larger blind spot along the coil axis, combined with inadequate signal-to-noise ratio, conspire to prevent imaging over the complete depth of the square feature. Coil ‘6’, and also ‘7’, not only performed poorly with regard to delivering good depth resolution, but these two coils caused some amount of feature magnification—since the image widths significantly exceed the feature dimensions by $\sim 50\%$. In all cases, there is some measure of solution overshoot, inasmuch as conductivities

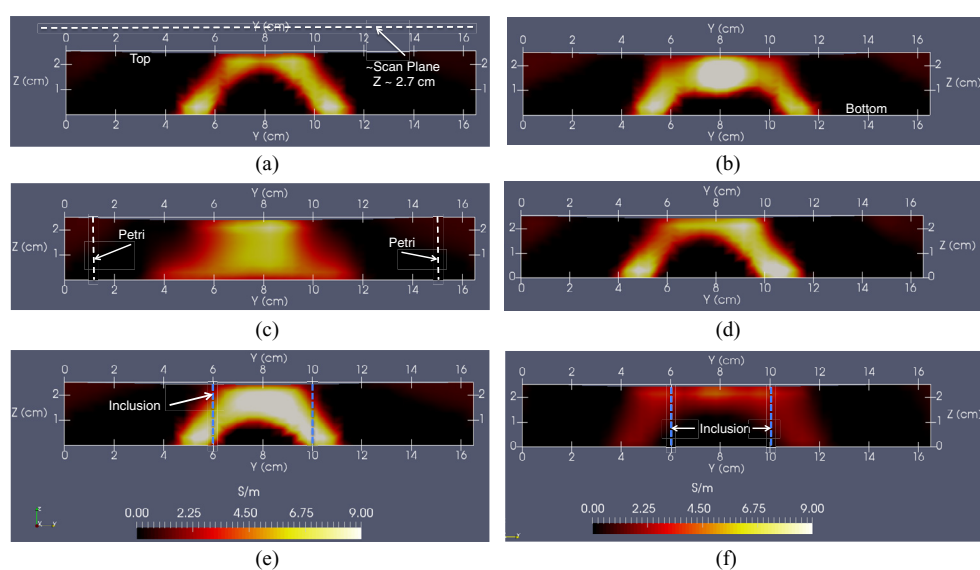


Figure 6. X-normal slices taken near $X = 8$ cm; (a) coil '1'; (b) coil '2'; (c) coil '3'; (d) coil '4'; (e) coil '5'; (f) coil '6'.

throughout the square feature exceed the measured conductivity of the square plug, which is 4.3 S m^{-1} . Surprisingly, coil '6' displays the least amount of overshoot, as indicated by the conductivity scale. Nonuniform permittivity may contribute to overshoot, since agarose and Play-DohTM materials have different relative permittivities (75 and 35 respectively). However, we note that there is some overshoot even with virtual phantoms where permittivity is perfectly uniform (Feldkamp 2017). Thus, its appearance here is more likely numerical in origin as a consequence of the very large and sudden jump in conductivity, from near zero to 4.3 S m^{-1} .

Z-normal slices for each of the coils, except again for '7', are shown in figure 7, with slices in each case acquired at mid-depth, or ~ 1.2 cm. Only coil '2' provides a faithful reconstruction of the central feature at mid-depth, predicting its correct size, and to some extent its square geometry. Slices acquired with three of the coil designs ('1', '5', '6') show a pronounced 'hole' in the center of the image, which can be ascribed to the blind spots associated with these coils, as indicated in figure 2. But again, improvements in signal-to-noise ratio could help to mitigate this issue since clearly, the ability of these three coils to generate eddy currents along their axes is lacking—and moving them off to the side does not help since the central feature in this phantom is surrounded by matrix having a $40 \times$ lowered conductivity. Ordinarily, we do not expect healthy tissues in the body to show this extreme variation in conductivity. However, in the event that malignant tissues form, as for breast tissue, conductivity variation might be as high as 10-fold (Joines *et al* 1994). Thus, in the next section, we examine a more complex phantom, consisting of two conductive squares, surrounded by nearly non-conductive matrix. Only coil '2' is considered.

8. Results for double-feature phantom

Our second phantom provides a more challenging test for conductivity imaging given the smaller conductivity of the embedded square features, as well as the fact that permittivity now

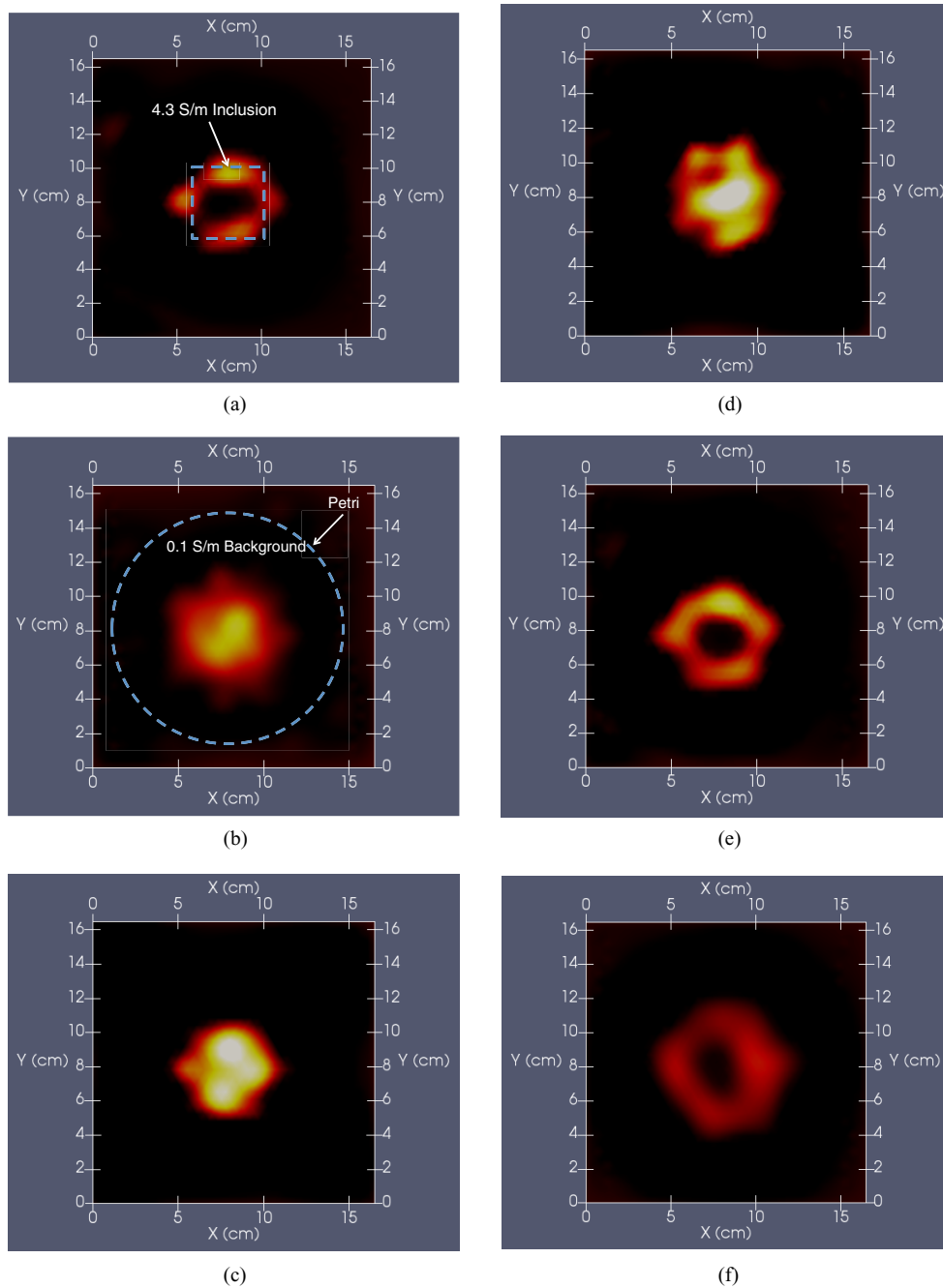


Figure 7. Z-normal slices taken near $Z = 1.2$ cm (mid-depth); (a) coil '1'; (b) coil '2'; (c) coil '3'; (d) coil '4'; (e) coil '5'; (f) coil '6'; refer to figure 6 for color scale.

changes considerably throughout the phantom—a violation of the uniform relative permittivity approximation used to arrive at equation (1). The change in the imaginary part of conductivity upon traversing the boundary between salt-doped agarose and fat is $\epsilon_o \omega \delta \epsilon_{rel} \approx 0.05 \text{ S m}^{-1}$ at 12.5 MHz, which is quite a bit smaller than the change in the real part of conductivity

(1.0 S m^{-1}), so any effect should be minor. Nevertheless, the possibility of a contrast error exists, so images in this section are examined for its presence. Furthermore, the gap distance between conductive squares is just under 2 cm, which provides a feature even smaller than the square plugs—a feature dimension shown to be resolvable in MIT work reported by Karbeyaz and Gencer (2003). Of interest is whether or not the near zero conductivity matrix separating the two conductive squares can be resolved over its full depth.

Figure 8 shows a sequence of Z-normal slices, beginning with a slice near the upper surface and then continuing with slices at depth increments of 0.2 cm. These continue until the deepest slice is reached at 1.0 cm, which is ~ 0.3 cm beneath the mid-plane of the phantom. The two conductive square features remain resolved up to a depth of 1.4 cm. Slices at deeper locations show the two squares merging together, which is partially due to inadequate signal-to-noise performance, though excluding measurements more distant from the target during the scan may also contribute. For all slices, conductivity of the squares tends to be mostly below the known value of 1.0 S m^{-1} , which may be a manifestation of the anticipated contrast error—in this case a contrast reduction, which is anticipated from our other work (Feldkamp and Quirk 2017a).

9. Discussion, conclusions and next steps

A number of single-coil designs, each having a geometry governed by the convolution integral of equation (1), were built on multi-layer PCB's and tested for their ability to resolve various conductive features built into laboratory phantoms. A careful examination of the convolution kernel reveals that each coil has a blind spot, a region along the coil axis where sampling is limited, or from a physical point of view, where eddy current generation is expected to be weak. Faithful reconstruction of structure cannot be expected in regions where eddy current generation is persistently weak—at least with our current instrumentation, reconstruction algorithm or scanning methodology.

To investigate the role of blind spots, our coils were designed to vary considerably in that regard, so that imaging performance is expected to vary as well. Furthermore, scanning had limited coil positioning to a single plane just above the target so as to amplify performance differences. Comparison of all seven coils suggests that improved performance is greatly dependent upon blind spot reduction and perhaps even exquisitely sensitive to blind spot size at some threshold, as suggested by the abrupt 'hole closure' upon going from coil '4' to '3' and then to '2'. Surprisingly, only one of the coils succeeded in fully resolving the higher-conductivity square features embedded in the phantoms, coil '2', which has the smallest blind spot of all coil codes. This result is likely due in part to signal-to-noise (S/N) limitations in current electronics, so that more of the coil designs might show improved performance if S/N were increased. But without S/N improvement, performance might be improved further by modifying design '2' to consist of smaller loop radii, or perhaps going to a single smaller loop radius, but with 6 layers rather than 4. There could even be some advantage to testing designs that assign more layers to innermost loops and fewer to outer loops so as to balance the spatial creation of eddy currents. In any event, the structure of the convolution kernel is shown here to provide a powerful tool for guiding the design of coils used in single-coil MIT.

Still another alternative is to combine scan data, obtained with different coils, during image reconstruction. Those coils which have a minimal blind spot might compensate for the much larger deficiencies of coils having a large blind spot. That is in fact where we intend to go next, once the image reconstruction algorithm is modified to accommodate scan data from multiple coil types. Target phantoms tested here contain features that span the entire thickness

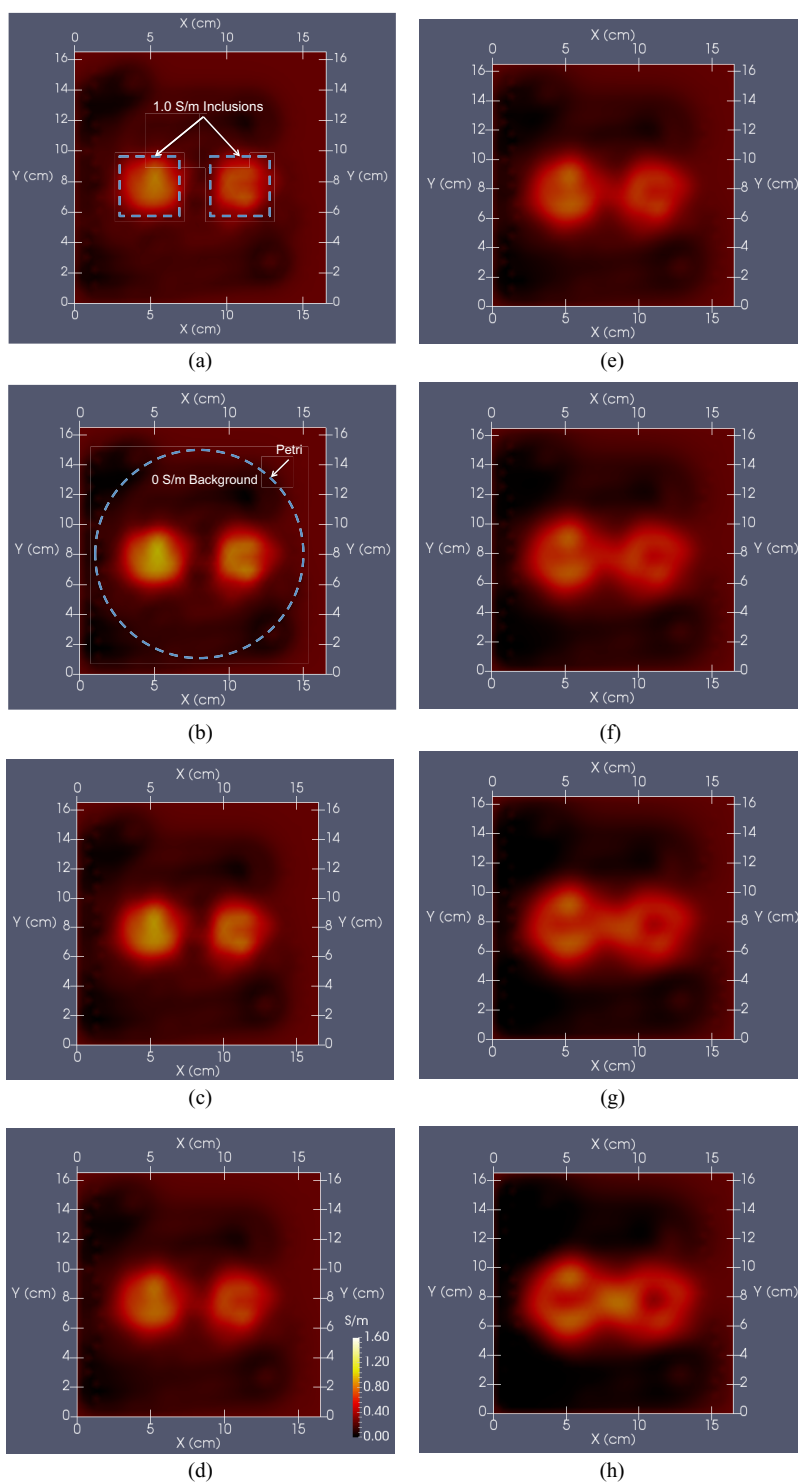


Figure 8. Z-normal slices for 2-feature phantom with coil ‘2’ at Z: (a) 2.4 cm (near top); (b) 2.2 cm; (c) 2.0 cm; (d) 1.8 cm; (e) 1.6 cm; (f) 1.4 cm; (g) 1.2 cm; (h) 1.0 cm (beneath mid-plane).

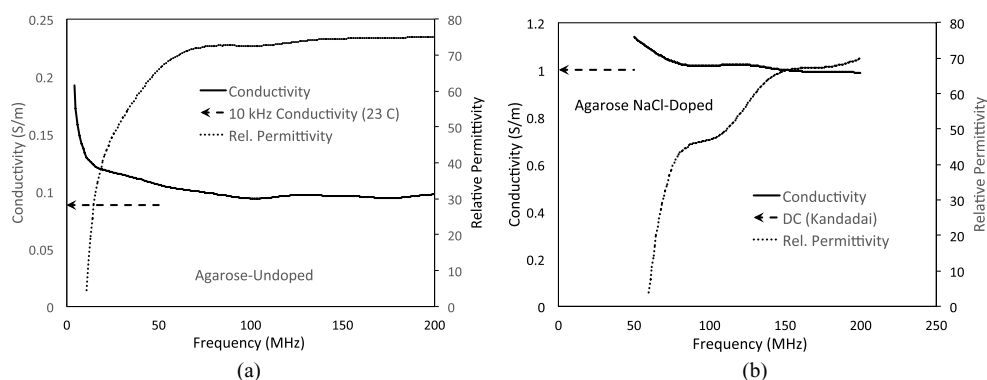


Figure A1. VHF electrical properties of Agarose; (a) 1.4% w w⁻¹ Agarose in distilled water; (b) Agarose doped with NaCl; values beneath ~75 MHz are not accurate due to test fixture and cable limitations.

of a phantom. So in order to more rigorously test alternative designs or combinations of coil designs during image reconstruction, our intent is to devise phantoms that contain fully buried features so that localization performance can be compared for newer coil designs or scan combinations.

Appendix. Independent conductivity measurements

Phantom component electrical properties were measured at low frequency (~10 kHz) and in the VHF region (above ~60 MHz). Low frequency conductivity was measured using a standard four-point method, while properties in the VHF region of the spectrum were measured on an Agilent Technologies ENA series, model E5071C network analyzer, using a flat-ended coaxial probe fixture. Due to cable and test fixture limitations, measurements made with the network analyzer are not accurate below ~60 MHz, which is evident in the attached plots of relative permittivity. Nevertheless, measurements at low frequency and in the VHF region indicate similar conductivities—0.1 S m⁻¹ for undoped agarose and 1.0 S m⁻¹ for doped agarose.

Similarly, measurements at either high or low frequency for various colors of Play-Doh™ agree with each other—low frequency conductivity measured using the four-point method is ~4.3 S m⁻¹, while VHF conductivity is about 4.1 S m⁻¹. Play-Doh™ permittivity in the VHF region is ~35.

References

- Al-Zeibak S and Saunders N H 1993 A feasibility study of *in vivo* electromagnetic imaging *Phys. Med. Biol.* **38** 151–60
- Dekdouk B, Ktistis C, Armitage D W and Peyton A J 2016 Absolute imaging of low conductivity material distributions using nonlinear reconstruction methods in MIT *Prog. Electromagn. Res.* **155** 1–18
- Delonzor R, Spero R K and Williams J J 2011 The electrical conductivity of *in vivo* human uterine fibroids *Int. J. Hyperth.* **27** 255–65
- Donatelli M, Neuman A and Reichel L 2012 Square regularization matrices for large linear discrete ill-posed problems *Numer. Linear Algebr. Appl.* **19** 896–913

- Feldkamp J R 2015 Single-coil magnetic induction tomographic three-dimensional imaging *J. Med. Imaging* **2** 013502
- Feldkamp J R 2017 Inversion of an inductive loss convolution integral for conductivity imaging *Prog. Electromagn. Res. B* **74** 93–107
- Feldkamp J R and Quirk S 2016 Effects of tissue heterogeneity on single-coil, scanning MIT imaging *Proc. SPIE 9783, Med. Imaging: Physics of Medical Imaging* (<https://doi.org/10.1117/12.2216805>)
- Feldkamp J R and Quirk S 2017a Validation of a convolution integral for conductivity imaging *Prog. Electromagn. Res. Lett.* **67** 1–6
- Feldkamp J R and Quirk S 2017b Optically tracked, single-coil, scanning magnetic induction tomography *Proc. SPIE 10132, Medical Imaging: Physics of Medical Imaging* (<https://doi.org/10.1117/12.2254435>)
- Feldkamp J R and Quirk S 2017c Optically tracked, single coil, scanning magnetic induction tomography *J. Med. Imaging* **4** 023504
- Gabriel S, Lau R W and Gabriel C 1996 The dielectric properties of biological tissues: II. Measurements in the frequency range 10 Hz to 20 GHz *Phys. Med. Biol.* **41** 2251–69
- Gradshteyn I S and Ryzhik 1980 *Table of Integrals, Series and Products* ed A Jeffrey (New York: Academic) (Corrected and enlarged edition)
- Griffiths H, Stewart W R and Gough W 1999 Magnetic induction tomography. A measuring system for biological tissues *Ann. New York Acad. Sci.* **873** 335–45
- Gürsoy D and Scharfetter H 2009 The effect of receiver coil orientations on the imaging performance of magnetic induction tomography *Meas. Sci. Technol.* **20** 105505
- Harpen M D 1988a Influence of skin depth on NMR coil impedance. Part II *Phys. Med. Biol.* **33** 597–605
- Harpen M D 1988b Influence of skin depth on NMR coil impedance *Phys. Med. Biol.* **33** 329–37
- Health Quality Ontario 2016 Magnetic resonance imaging as an adjunct to mammography for breast cancer screening in women at less than high risk for breast cancer: a health technology assessment *Ont. Health Technol. Assess. Ser.* **16** 1–30
- Hoult D I and Lauterbur P C 1979 The sensitivity of the zeugmatographic experiment involving human samples *J. Magn. Reson.* **34** 425–33
- Hruska C B 2017 Molecular breast imaging for screening in dense breasts: state of the art and future directions *AJR Am. J. Roentgenol.* **208** 275–83
- Joines M T, Zhang Y, Li C and Jirtle R L 1994 The measured electrical properties of normal and malignant human tissues from 50 to 900 MHz *Med. Phys.* **21** 547–50
- Jones B 1993 Resistance measurements on Play-Doh™ *Phys. Teach.* **31** 48–9
- Kandadai M, Raymond J L and Shaw G J 2012 Comparison of electrical conductivities of various brain phantom gels: developing a brain gel model *Mater. Sci. Eng. C* **32** 2664–7
- Karbeyaz B U and Gencer N G 2003 Electrical conductivity imaging via contactless measurements: an experimental study *IEEE Trans. Med. Imaging* **22** 627–35
- Korjenevsky A, Cherepenin V and Sapetsky S 2000 Magnetic induction tomography: experimental realization *Physiol. Meas.* **21** 89–94
- Kuhn H W and Tucker A W 1951 Nonlinear programming *Proc. of 2nd Berkeley Symp.* (Berkeley, CA: University of California Press) pp 481–92
- Lam D L, Houssami N and Lee J M 2017 Imaging surveillance after primary breast cancer treatment *AJR Am. J. Roentgenol.* **208** 676–86
- Lapidus L and Pinder G F 1982 *Numerical Solution of Partial Differential Equations in Science and Engineering* (New York: Wiley)
- Peyton A J *et al* 1996 An overview of electromagnetic inductance tomography: description of three different systems *Meas. Sci. Technol.* **7** 261–71
- Rhee S J, Han B K, Ko E S, Choi J S and Ko E Y 2017 An audit of the results of ultrasound-guided core needle biopsy of mammography versus ultrasound screen-detected breast lesions *J. Clin. Ultrasound.* **45** 261–6
- Scharfetter H, Hollaus K, Rossell-Ferrer J and Merwa R 2006a Single-step 3D image reconstruction in magnetic induction tomography: theoretical limits of spatial resolution and contrast to noise ratio *Ann. Biomed. Eng.* **34** 11 1786–98
- Scharfetter H, Brunner P and Merwa R 2006b Magnetic induction tomography: single-step solution of the 3D inverse problem for differential image reconstruction *Int. J. Inform. Syst. Sci.* **2** 4 585–606
- Stawicki K and Gratkowski S 2010 Optimization of signal coils in the magnetic induction tomography system *Prz. Elektrotech.* **86** 74–7

- Wang H, He Y, Yang M, Yan Q, You F, Fu F, Wang T, Huo Z, Dong X and Shi X 2014 Dielectric properties of human liver from 10 Hz to 100 MHz: normal liver, hepatocellular carcinoma, hepatic fibrosis and liver hemangioma *Bio-Med. Mater. Eng.* **24** 2725–32
- Wei H Y and Soleimani M 2013 Electromagnetic tomography for medical and industrial applications: challenges and opportunities *Proc. IEEE* **101** 559–64
- Wei H Y and Soleimani M 2012 Three-dimensional magnetic induction tomography imaging using a matrix free Krylov subspace inversion algorithm *Prog. Electromagn. Res.* **122** 29–45
- Wiles A D, Thompson D G and Frantz D D 2004 Accuracy assessment and interpretation for optical tracking systems *Med. Imaging Proc. (SPIE)* **5367**
- Zaman A J M, Long S A and Gardner C G 1980 The impedance of a single-turn coil near a conducting half space *J. Nondestruct. Eval.* **1** 183–9